In-Flight Pose and Electromagnetic Experimental Characterization of UAV-Mounted Metasurfaces for Next-Generation Indoor Wireless Systems

Enrico Boffetti*, *Graduate Student Member, IEEE,* Ilaria Marasco*, *Member, IEEE,* Carla Cantore, *Graduate Student Member, IEEE,* Giovanni Magno†, *Member, IEEE,* Giuseppe Piro, *Member, IEEE,* Antonella D'Orazio, *Member, IEEE,* Luigi Alfredo Grieco, *Member, IEEE,* Gennaro Boggia, *Member, IEEE*
* Co-first authors
† Corresponding author

***Abstract*—As well known, the integration of Unmanned Aerial Vehicles (UAVs) and Intelligent Reflecting Surfaces (IRS) can enhance the reliability, coverage, robustness, and efficiency of next-generation wireless and mobile networks. Nevertheless, the performance of UAV-mounted Passive Metasurfaces (PMs), referred to as Aerial PMs (APMs), is significantly influenced by system configurations, electromagnetic signal propagation, UAV mobility, and wobbling. While most state-of-the-art studies rely on analytical models and simulations to assess these factors, this work presents an experimental investigation of an APM in a realistic operating environment. To this end, we developed an advanced experimental testbed that combines a precision tracking system with real-time electromagnetic measurements, enabling a detailed characterization of the metasurface response in an indoor scenario. Additionally, we compared the feasibility of APMs against a static setup where the metasurface is mounted on a fixed structure. Experimental results demonstrate that APMs can effectively maintain signal quality and spectral efficiency. However, they also reveal the impact of positioning, orientation, and in-flight stability on overall system performance. Our observations provide interesting insights into optimizing Aerial IRS-assisted networks, contributing to the design of more robust solutions for the Beyond 5th and 6th Generation networks.**

***Index Terms*—6G, IRS, UAV, Experimental Testbed, Performance Evaluation**

I. Introduction

THE 6th Generation (6G) wireless networks are poised to revolutionize connectivity by delivering ultra-high data rates, global coverage, ultra-low latencies, and exceptionally high reliability. Academia and industry are exploiting novel technologies to meet these requirements while maintaining affordability, low complexity, and high Energy Efficiency (EE) [1]. In this scenario, low-cost Unmanned Aerial Vehicles (UAVs), operating at altitudes up to a few hundred meters, offers unprecedented flexibility thanks to their 3D maneuverability, enabling rapid position adjustments. Unlike fixed infrastructure such as antennas and cell towers, UAVs can be dynamically deployed to areas experiencing high demand or weak coverage, providing greater deployment flexibility and Line-Of-Sight (LOS) capability [2]. These features make UAVs suitable for establishing rapid on-demand LOS connections in scenarios such as multi-robot communications, emergency communications, and rescue operations [2]–[4]. Despite these advantages, UAV-aided communications face some challenges. First, being battery-powered, their operational time is limited, typically from a few minutes to a few hours [5]. Also, it faces blockage from obstacles, time-varying channel due to UAVs and ground users' mobility, and degrades channel quality with increasing distance between UAVs and connected devices. Therefore, optimizing UAV flight paths and resource allocation is crucial to achieving performance while reducing energy consumption and computational overhead in UAV-aided networks [6].

Integration of UAVs with Intelligent Reflective Surfaces (IRSs) or Passive Metasurfaces (PMs) efficiently improves network coverage and communication quality [1], [3], [5]. In this discussion, we will distinguish different entities: Aerial IRS (AIRS) refers to a tunable IRS mounted on UAV, while Aerial Passive Metasurface (APM) denotes a UAV carrying a non-tunable PM; similarly IRS and PM indicate spatially fixed structures. PMs and IRSs are ultra-thin structures composed of fixed or programmable unit cells, respectively, engineered to control electromagnetic wave properties such as absorption, reflection, refraction, and polarization. Each unit cell can independently or collectively manipulate the signal's amplitude, phase, and frequency, allowing the metasurface to steer, redirect, split, or intensify electromagnetic signals in selected directions without extra energy expense [1], [7]. While both IRSs and PMs offer advanced wave manipulation capabilities, they differ in terms of trade-offs such as weight, design com-

Manuscript received XX XXX XXXX; This work was supported by the European Union under the Italian National Recovery and Resilience Plan (NRRP) of NextGenerationEU, Mission 4, Component 2, in the context of partnership on "Telecommunications of the Future" (PE00000001 - program "RESTART", CUP: D93C22000910001), national center on "Sustainable Mobility" (CN00000023 - program "MOST", CUP: D93C22000410001), and partnership on "Cybersecurity" (PE00000007 - program "SERICS", CUP: D33C22001300002, project ISP5G+). It was also supported by the PRIN 2022 projects INSPIRE (grant no. 2022BEXMXN 01) and HORUS (grant no. 2022P44KA8) funded by the Italian MUR, and by the HORIZON MSCA project BRIDGITISE (grant no. 101119554). (Corresponding author: Giovanni Magno.).

Enrico Boffetti, Ilaria Marasco, Carla Cantore, Giovanni Magno, Giuseppe Piro, Antonella D'Orazio, Luigi Alfredo Grieco, and Gennaro Boggia are with the Department of Electrical and Information Engineering, Politecnico di Bari, 70125 Bari, Italy, and also with the Consorzio Nazionale Interuniversitario per le Telecomunicazioni, Pisa, Italy (e-mail: giovanni.magno@poliba.it).

plexity, energy consumption, and control requirements, which should be carefully considered depending on the application scenario. PMs, which function as fixed-state non-powered IRSs, align with smart city sustainability goals by offering improved cost-/energy-effectiveness compared to active IRSs. When mounted on UAVs, APMs operate as mobile relays that extend the range of existing Base Station (BS) by flying over obstacles. In contrast, UAVs serving as aerial BS typically use active antennas that drain batteries, whereas low-consumption, lightweight IRSs offer a more energy-efficient solution for controlling the propagation environment [8]. These features make APMs suitable for enhancing connectivity in warehouses and logistics centers. Industrial environments with complex geometries, numerous obstacles (e.g. metal structures, dense racking, machinery), and a high Internet of Things (IoT) devices and automation systems density cause Non-Line-Of-Sight (NLOS), multi-path effects, and interference that degrade wireless communications performance. To mitigate these issues, an innovative solution is to deploy an AIRS, which establishes LOS communication between nodes and significantly improves the wireless environment.

In these scenarios, AIRS reflect BS signals to mobile users, establishing concatenated virtual LOS links that bypass obstacles. These links can share the same frequency, enhancing network spectral efficiency [9].

Field trials in real-world environments are essential to validate the feasibility of this emerging technology. Several experimental investigations on indoor communication systems using fixed IRSs are available [10]–[13]. For example, Kayraklık et al. [10] evaluated the effect of an IRS on the signal received through an L-shaped hallway. Instead, [11] analyzes the power received by a user located in a blind spot from the transmitter. Additionally, [12] investigated scenarios including (i) an open lobby with mixed LOS and NLOS conditions, (ii) corridor junctions, and (iii) multi-floor propagation via windows. Finally, [13] experimentally investigates a large-scale indoor environment (a full building floor with five large corridors) demonstrating that a passive metasurface significantly improves Wi-Fi coverage.

Nonetheless, to the best of our knowledge, similar trials for systems relying on APMs are lacking. This paper aims to bridge this gap by providing a comprehensive analysis of APMs electromagnetic behavior in indoor environments, with a specific focus on how UAV position shifts affect the system's electromagnetic response.

As illustrated in Fig. 1, autonomous warehouses require continuous communication between robots to prevent collisions, coordinate tasks, and exchange critical data. In these dynamic settings, AIRSs enable real-time adaptive connectivity.

The main novelties introduced by this paper to the existing literature are:

- development of a fully synchronized experimental setup to deepen the study of APM and quantify the impact of UAV effects (e.g., wobbling, vibrations, etc.) along with an analysis aimed at identifying possible mitigation strategies;
- comprehensive electromagnetic system characterization through a comparative performance analysis between APM and fixed PM in an indoor scenario.

The paper is organized as follows. Section II reviews related work on AIRSs and APMs. Section III describes the research motivations and organization. Section IV details the hardware components used in the experimental setup. Section V outlines the key systems for the metasurface experimental characterization. Section VI presents the results, comparing fixed and flight scenarios. Finally, Section VII concludes the paper and suggests future developments.

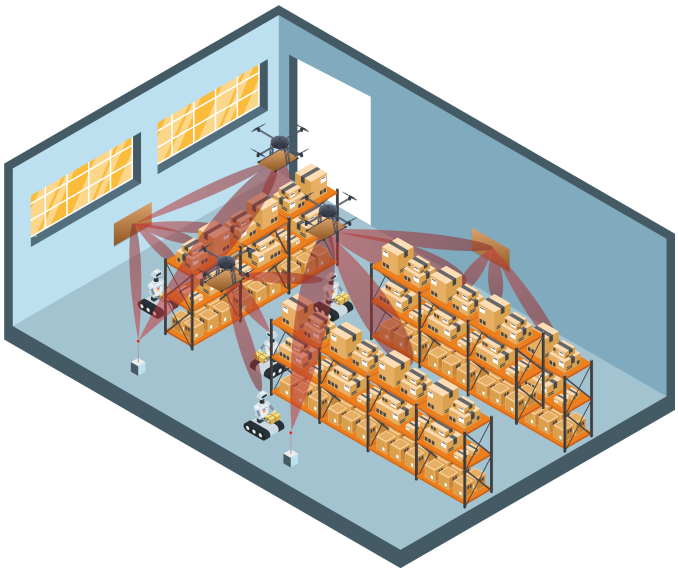

Fig. 1. APMs and fixed-PM communication in a warehouse indoor scenario.

II. Related Work

Integrating UAV with metasurfaces fully discloses the strengths of both technologies. By dynamically adjusting UAV real-time position and intelligently tuning metasurface amplitudes and phase shifts, favorable propagation conditions can be established. Numerous studies focus on fixed IRS deployment (e.g., on building facades) and propose various optimization techniques. For example, [6], [14], [15] introduce algorithms for maximizing communication rate via a joint optimization of IRS passive beamforming and UAV trajectory. Moreover, the integration of other physical layer technologies (e.g, Orthogonal Frequency Division Multiple Access (OFDMA) [18], Non-Orthogonal Multiple Access (NOMA) [19], [20], millimeter wave (mmWave) [21], and Terahertz (THz) communications [22]) is also explored to further enhance connectivity or security [14], [21], [23].

However, this fixed architecture shows several limitations [3], [5]. Installing IRSs raises practical concerns in both outdoor (e.g., site rent, urban landscape impact) and indoor scenarios (e.g., surface functionality, aesthetics). From a performance standpoint, fixed IRSs can only serve users located on the same side of the metasurface. In complex, obstructed environments, signals may require multiple reflections to reach the destination node, significantly reducing their strength.

TABLE I
COMPARISON OF RELATED WORK ON IRS-AIDED COMMUNICATION SYSTEMS.

Reference	Type of study	IRS Placement	Optimization	Wobbling study	Ideal IRS	Real-Time Measurements	
						Pose Tracking	Power Level
[6], [14]–[23]	Simulative	Fixed	✓	✗	✓	✗	✗
[9], [24]	Simulative	Fixed & Aerial	✓	✗	✓	✗	✗
[25]–[33]	Simulative	Aerial	✓	✗	✓	✗	✗
[34]	Analytical	Aerial	✗	✗	✓	✗	✗
[35]	Simulative & Analytical	Aerial	✓	✗	✓	✗	✗
[36]–[38]	Simulative	Aerial	✓	✗	✓	✗	✗
[8], [39]	Simulative	Aerial	✓	✓	✓	✗	✗
[40]–[42]	Analytical	Aerial	✓	✓	✓	✗	✗
[43]	Simulative	Aerial	✗	✗	✓	✗	✗
[44]	Simulative & Analytical & Experimental	Fixed	✗	✗	✗	✗	✗
[45]	Analytical & Experimental	Aerial	✗	✓	✗	✗	✓
Our Work	**Simulative & Experimental**	**Fixed & Aerial**	✗	✓	✗	✓	✓

In such cases, AIRSs, with the IRS installed on an aerial platform, are more effective. Their elevated position facilitates the establishment of LOS links with NLOS users, enabling the signal to be delivered via a single reflection.

Numerical studies of mmWave downlink transmissions [9] demonstrate the superiority of AIRS over fixed IRS systems, showing improved average data rate and enhanced LOS probability, while [24] demonstrates enhanced EE compared to traditional amplify-and-forward relay systems. These promising results have catalyzed extensive research in AIRS that focuses on optimizing various performance metrics, such as EE [28], [35], Spectral Efficiency (SE) [35], achievable rate [36], Signal-to-Noise Ratio (SNR) [25], throughput [26], channel gain [37], UAV endurance [27], and security [28]–[30], [38]. Other studies incorporate additional physical layer techniques into AIRS-assisted networks, such as NOMA [31]–[33]. Finally, in [34], [35], mathematical frameworks have been developed to assess AIRSs in terms of outage probability, Bit Error Rate (BER), average sum rate, ergodic capacity, and EE.

A key aspect that stems from the literature review is the synergistic relationship between UAVs and IRSs: UAVs provides mobility to IRSs, while IRSs enable UAVs to adapt to real-time environment changes, breaking new ground in UAV-aided communication. However, jointly optimizing UAV placement and IRS phase shifts increases costs and power consumption. A cost-effective solution, as suggested in [43], consists of deploying inexpensive PMs on UAVs. Nonetheless, both AIRS and APMs experience larger channel fluctuations compared to fixed installations due to their mobility. AIRSs are impacted by UAV jittering from atmospheric conditions (e.g., wind) and vibrations, leading to alterations in UAV trajectory and speed and, ultimately, unstable transmission. Despite this, most studies assume stable UAV flight and ideal IRS phase shift distribution, presuming they can perfectly manipulate electromagnetic waves. Only a few papers have numerically investigated UAV wobbling impact on AIRSs design optimization [8], [39]–[42]. Besides, it is worth pointing out that metasurface response is typically highly sensitive to the angle of incidence [44]. Therefore, their positioning and orientation must be properly chosen to align with the incoming signal and desired outgoing direction, requiring an accurate positioning system.

Accurately modeling the metasurface response poses a further challenge in these scenarios. Most studies rely on simplified mathematical models representing the IRS as a diagonal matrix of phase shift values; however, factors such as metasurface size, near-/far-field effects [44], and mutual coupling between unit cells [46], significantly affect its behavior.

In [45], a theoretical analysis assesses the impact of UAV mobility (including positioning, alignment, and orientation) on absorbing metasurfaces link performance. The study models path loss between transmitter and receiver antennas pointing towards the metasurface. Theoretical findings were validated through experimental measurements conducted by manually "flying" the UAV-mounted metasurface in an anechoic chamber. To assess the mobility-induced fluctuations of the path loss, scattering parameters were measured over time during a UAV flight.

Table I summarizes the main differences between this work and previously reviewed studies. In detail, most of the existing literature focuses on simulative and/or analytical analyses [6]–[44]. Concerning them and in light of the above considerations, we experimentally and comprehensively analyze the impact of the entire system, also considering drifts and vibration of UAV, metasurface design, channel characteristics, and beam misalignments on a link relying on a APM. Additionally, we investigate possible mitigation strategies to counteract these effects and improve overall system robustness. To the best of the author's knowledge, we report for the first time a full characterization of an indoor APM link, analyzing the impact of UAV movement, oscillations, and metasurface electromagnetic behavior.

III. RESEARCH MOTIVATIONS AND CONTRIBUTIONS

The literature review revealed that current solutions predominantly focus on outdoor scenarios, with limited studies and analyses on the application of these technologies in indoor environments. However, indoor spaces are highly dynamic and require flexible solutions for wireless environment reconfiguration. For instance, in a fully autonomous warehouse operated by cooperating robots, as illustrated in Fig. 1, continuous network coverage is essential to prevent collisions, share telemetry data, and exchange real-time information about the warehouse's status. Given the dynamic nature of such an

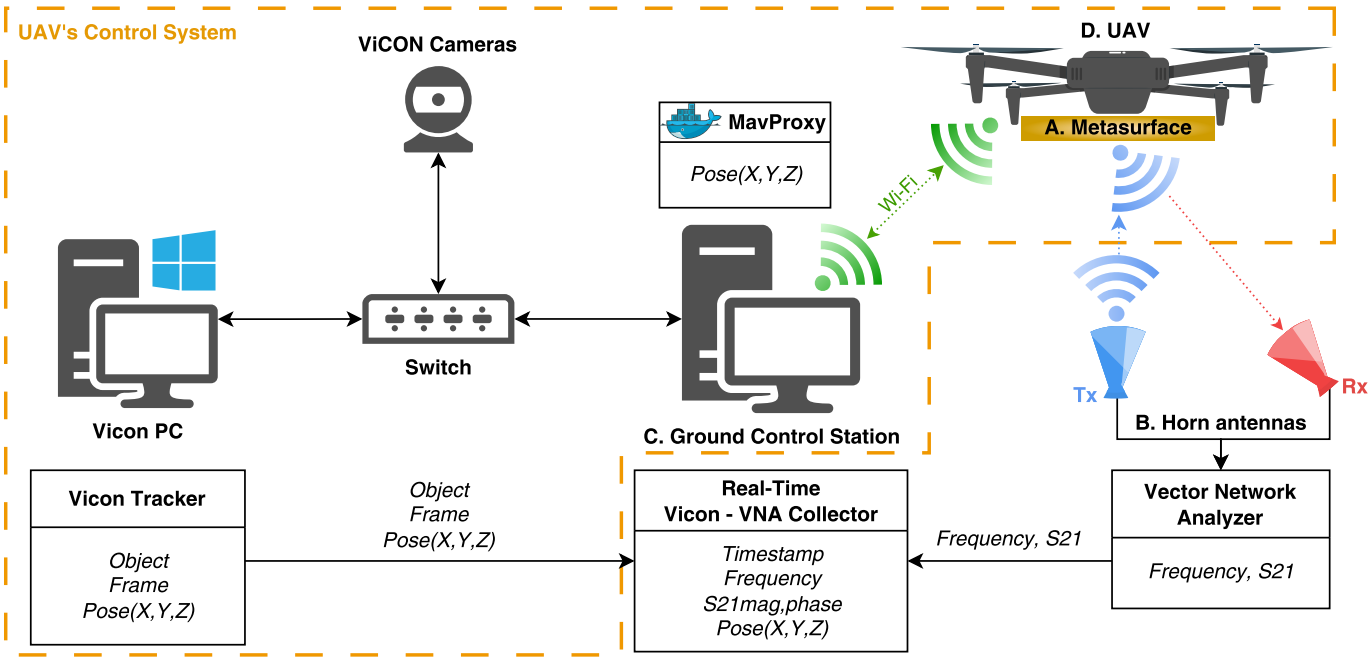

Fig. 2. Scheme of the developed, deployed, and investigated system illustrating the different entities and their relationships in a UML-like diagram.

environment, AIRSs and APMs offer a promising solution by enabling real-time environment reconfiguration.

Our paper is the first in the literature to analyze these indoor scenarios and assess their performance, through the development of an integrated experimental setup, as illustrated in Fig. 2. The APM system is characterized via the scattering parameter S_{21}, measured by using two horn antennas (one acting as the transmitter (Tx) and the other as the receiver (Rx)) connected to a Vector Network Analyzer (VNA).

To obtain the pose information (i.e., position and orientation) of objects, a motion capture system was employed. This system features multiple cameras positioned around the entire perimeter of the measurement environment to ensure complete visual coverage. Pose and Electromagnetic data are jointly collected in an integrated and synchronized manner by the Ground Control Station (GCS) using a custom-developed module.

The purpose of this setup is to evaluate the electromagnetic response of an APM including the effect of the flight in a controlled indoor scenario. To facilitate interpretation of the results, they will be compared to those obtained by characterizing the same PM constrained to fixed spatial positions.

In this study, we adopt a PM in place of an IRS because, in addition to being regarded as a fixed programming of an IRS, it also offers significant advantages in both energy efficiency and simplicity, particularly in low-power or energy-constrained scenarios.

The organization of the forthcoming manuscript sections is described below. Section IV details the system's hardware components, beginning with the PM in Section IV-A, followed by horn antennas and the VNA specifications in Section IV-B. Sections IV-C and IV-D describe the GCS and the UAV, respectively, while Section V-A illustrates the UAV's control system. Section V describes the integrated setup software components: the position tracking system is detailed in Section V-B, the electromagnetic measurement system in Section V-C, and the real-time Vicon-VNA collector in Section V-D.

Using this setup, the analysis presented in Section VI follows four main steps:

1) the characterization of the fixed PM is provided in Section VI-A;
2) the impact of pose on the electromagnetic behavior of the system is presented in Section VI-B;
3) the comparison of results obtained from the fixed and APM systems is reported in Section VI-C;
4) the 3D spatial characterization of the environment is outlined in Section VI-D.

Our findings highlight the performance differences between the fixed PM and APM scenarios, providing details on how UAV vibration, wobbling, and displacement affect the system. The fixed PM demonstrated good agreement between simulated predictions and experimental measurements.

IV. Hardware Components

A. Metasurface

The PM used in our tests consists of three layers: an FR-4 dielectric substrate sandwiched between two 35 μm-thick copper layers. The dielectric has a thickness of 1.66 mm, with a permittivity (ϵ) of 4.4 and a loss tangent (tanδ) of 0.002. A ground plane at the bottom of the substrate serves as a mirror. The top layer consists of a patterned array of 10 x 10 supercells, each comprising 11 phase-delaying elements, as depicted in Fig. 3. The numerical analysis of the metasurface was conducted using CST Studio [47] frequency domain solver, employing a full-wave approach within the 8-12 GHz range. The metasurface was excited by a normally incident

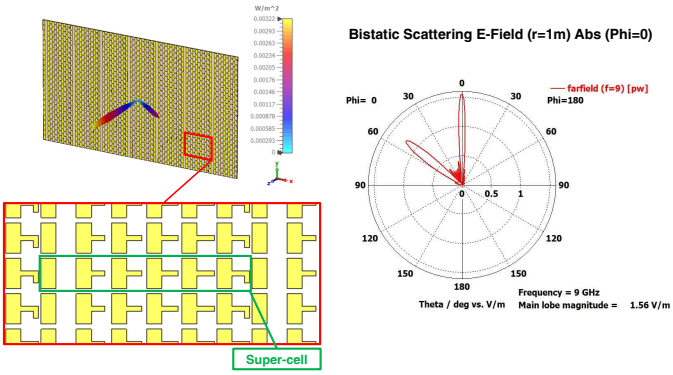

Fig. 3. Sketch of the metasurface with a magnified detail of a group of supercells. The reflected power flow is depicted as a 3D polar pattern, superimposed on the metasurface. Bottom left: polar pattern of the electric field magnitude at the working frequency.

TE-polarized plane wave. Numerical results show that, at the design frequency of 9 GHz, a reflected wave emerges at an angle of 52° (with reciprocal behavior due to system reciprocity). The metasurface was fabricated using an LPKF Protomat S104 system.

B. Horn antennas and Vector Network Analyzer

The experimental setup employed two X-band (8.2-12.4 GHz) aluminum horn antennas from Arra Inc., with rectangular apertures measuring 6.68 cm (height) x 8.89 cm (width). These antennas provide gain values between 15 to 18 dBi. The two antennas have been connected to the VNA Keysight FieldFox N9917A.

C. Ground Control Station

The GCS is equipped with an AMD Ryzen Threadripper Pro 5965WX processor, featuring 24 cores and 48 threads, with a base clock of 3.8 GHz and a maximum boost clock of 4.5 GHz. The system includes 128 GB (4x32GB) DIMM DDR4 RAM at 3200 MHz. The system is equipped with an ASUS TUF NVIDIA GeForce RTX 4070 Ti graphics card featuring 12 GB of dedicated VRAM. For storage, it incorporates a 1 TB Samsung 980 Pro M.2 SSD. The motherboard is an Asus Pro WS WRX80ESAGE SE WIFI II, featuring the WRX80 chipset and sWRX8 socket, with 7 PCIe 4.0/3.0 x16 slots, dual 10 Gb Ethernet interfaces, Wi-Fi 6, Bluetooth 5.2, and support for 10 USB rear ports and 7 front USB ports. Additionally, it includes two Intel E810-XXVDA4 network cards with Quad Port 10/25GbE SFP28. The installed operating system is Ubuntu 22.04.

The GCS utilizes Docker containers to implement the middleware interface between Vicon and the UAV, as described in Section V-A. Furthermore, the GCS manages data collection from the VNA and Vicon through the Real-Time Vicon-VNA Collector module, as detailed in Section V-D.

D. Unmanned Aerial Vehicle

As the primary aerial platform, a custom UAV was developed based on the Holybro X500 V2 kit. The flight control system is built around the Pixhawk 6C, a high-performance Flight Controller (FC) that ensures precise and reliable stabilization of the aircraft. The UAV operates on the ArduCopter firmware, an open-source, feature-rich software stack that provides advanced flight control.

For telemetry and communication, an ESP-8266 Wi-Fi module was integrated via the Pixhawk 6C serial port, enabling bidirectional data exchange between the UAV and the GCS. Furthermore, a custom firmware implementation was deployed to facilitate the direct acquisition of UAV pose data (i.e. the position and orientation) from the Vicon motion capture system.

A Proportional-Integral-Derivative controller was tuned to enhance flight stability and control accuracy. The calibration process involved iterative parameter optimization to refine the proportional, integral, and derivative gains.

V. Software Components

A. UAV's Control System

The Vicon Tracker software facilitates real-time capture and visualization of rigid body groups while simultaneously streaming position and rotation data to third-party applications. For this setup, we use IR VERO 2.2 Vicon cameras, which deliver 330 Frame Per Second (FPS) at a 2.2 MP resolution, ensuring high-precision tracking.

To adapt to indoor environments, we modified the ArduCopter firmware configuration running on the Pixhawk 6C FC, enabling Wi-Fi-based GPS functionality. This adjustment allows for seamless transmission of real-time pose data from the Vicon system to the UAV, eliminating the need for GPS satellites and making it ideal for indoor settings. To streamline communication between the Vicon system and the UAV, we adopted a Docker container-based architecture, leveraging the PyVICON and MavProxy libraries [48], [49]. The Vicon API is used to transmit pose data to the FC.

This integration allows the FC to process pose data from the Vicon system as if it were GPS signals, enabling precise positional control. We selected the Position Hold flight mode, which ensures stable positioning by maintaining the UAV's position even when no control commands are issued.

To support the metasurface integration onto the UAV, a custom 3D-printed mount was designed. The mount ensures that the metasurface remains fixed at a 0° inclination, maintaining optimal orientation and stability during the flight.

B. Position Tracking System

To obtain precise pose data for the distinct movable parts of the system (i.e., the two horn antennas, the UAV, and the metasurface), we utilized the Vicon motion capture system. The Vicon system offers exceptional positional tracking precision, with spatial position data estimated to an accuracy of 2 mm [50]. To recognize and track distinct entities, a unique Vicon object was defined for each system component by arranging reflective markers in distinctly different configurations.

Algorithm 1 Data Acquisition Process.

Data: Vicon position and tilt data, VNA S_{21} and frequency axis.
Result: Position, tilt and S_{21} for each frequency over time.
Initialization:
Set number of iterations: `j`
Set output file: `filename`
Initialize Vicon and VNA objects: `Vicon, VNA`
Set tracked object name (UAV): `subject`
Obtain position of horn antennas: `position_tx`, `position_rx`
Write file header to `filename`
Frequency Initialization:
Call `VNA.getS21` to measure S_{21}
Get frequency axis: `frequencies = VNA.getfreqs`
Acquisition Loop:
for *i to j* **do**
  Start Measure and timing:
  `start_measure_vicon = toc`
  `position_uav_a, tilt_uav_a = Vicon.get_pos_tilt(subject)`
  `start_measure_vna = toc`
  `S21mag, S21phase = VNA.getmagphase`
  Measure and end times:
  `stop_measure_vna = toc`
  `pos_uav_b, tilt_uav_b = Vicon.get_pos_tilt(subject)`
  `stop_measure_vicon = toc`
  Write time, frequencies, S_{21}, position, and orientation data to `filename`
end

In particular, the horn antennas were distinguished based on their inclination angles to facilitate role identification within the system. The Vicon system's precise tracking capabilities were crucial for monitoring dynamic changes in the spatial arrangement of the components, particularly during UAV operations, as well as ensuring proper system alignment. The reference systems under consideration are explicitly defined to analyze how the pose (i.e., the position and orientation of the rigid body) of the APM influences the system's electromagnetic behavior. In particular, the UAV's orientation is characterized by three rotation angles: θ_r around the longitudinal axis; θ_p around the transverse axis; and θ_y around the vertical axis, as illustrated in Fig. 4. According to its documentation, the Vicon system, via its Software Development Kit (SDK), specifies the orientation of objects using Euler angles. For the purposes of this paper, the Vicon reference frame will be utilized to represent the pose of all objects.

C. Electromagnetic Measurements

The experimental setup was subsequently utilized to evaluate the electromagnetic performance of the system, particularly focusing on the role of the PM in the signal propagation path. To achieve this goal, we analyzed the scattering parameter S_{21}, which comprehensively accounts for total losses, encompassing free-space losses and losses arising from the

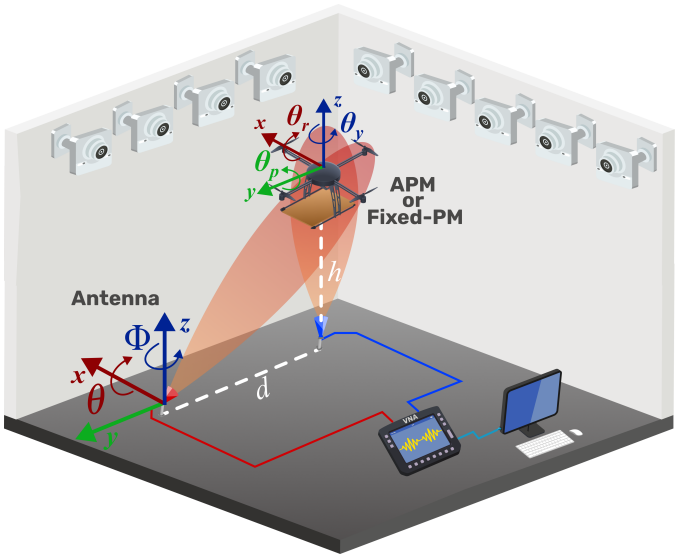

Fig. 4. Reference coordinate systems of the APM and Rx antenna, along with the involved hardware: the upper part features the Vicon cameras, which are connected to the Vicon PC. The middle part contains the APM/Fixed-PM system. The bottom part includes the Tx and Rx horn antennas, both connected to the VNA for measuring the S_{21} parameter. The VNA is linked to the GCS via an Ethernet cable.

interaction with the metasurface, including ohmic, scattering, and diffraction losses. The measurement process involves transmitting a signal via the VNA from the Tx antenna, which propagates through the air toward the PM. The latter interacts with the incident electromagnetic waves, reflecting them towards the Rx antenna that captures the resulting signal. The VNA then measures the scattering parameter S_{21} across a specified frequency range. The S_{21} represents the ratio of received to transmitted signal, whose magnitude quantifies signal attenuation between the Tx and Rx antennas. We calibrated the VNA with open, short, and load calibration standards to ensure measurement accuracy and repeatability. The horn antennas were aligned to maintain consistent LOS configuration and to maximize the power transfer between the Tx and Rx. The optimal antenna separation distance d was determined by maximizing the S_{21} parameter intensity according to the trigonometric relationship $d = h \cdot \cot(\theta)$, where $\theta = 52°$ is the inclination angle of the Rx antenna. Data acquisition was conducted over a specified frequency range from 8 to 12 GHz. The measured S_{21} parameters were recorded for multiple metasurface positions and orientations, enabling a thorough analysis of its impact on the transmitted signal.

D. Real-Time Vicon-VNA Collector module

The data acquisition process was implemented using MATLAB to collect synchronized and integrated data from the Vicon system and the VNA.

The process begins with the initialization of system objects for the Vicon and VNA interfaces: the tracked object (i.e., the APM) is initialized, and the positions of the horn antennas are recorded; the frequency range is obtained by retrieving the frequency axis from the VNA.

TABLE II
DEFINITION OF THE SYSTEM PARAMETERS.

Parameter	Description	Unit
$s_{t,y}$	Displacement of Tx along y-axis	cm
$s_{t,x}$	Displacement of Tx along x-axis	cm
$s_{r,y}$	Displacement of Rx along y-axis	cm
$s_{r,x}$	Displacement of Rx along x-axis	cm
$s_{m,x}$	APM/fixed-PM displacement along x-axis	cm
$s_{m,y}$	APM/fixed-PM displacement along y-axis	cm
$s_{m,z}$	APM/fixed-PM displacement along z-axis	cm
d	Linear distance between Tx and Rx	cm
h	Height of the metasurface above the Tx	cm
θ_r	Metasurface inclination angle relative to x-axis	deg
θ_p	Metasurface inclination angle relative to y-axis	deg
θ_y	Metasurface inclination angle relative to z-axis	deg
θ	Vertical inclination angle of Rx	deg
ϕ	Horizontal inclination angle of Rx	deg

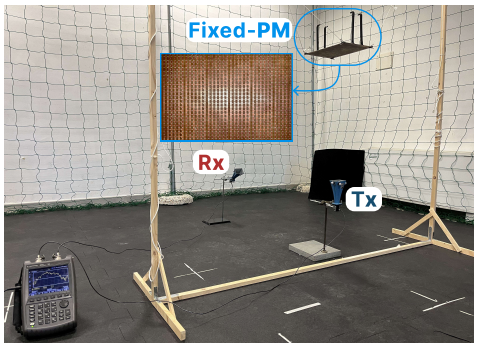

Fig. 5. Photograph of the setup implemented for fixed-PM measurement with a magnified detail of the fabricated metasurface.

The main acquisition loop iterates over a predefined number of cycles, during which the system retrieves the UAV-assisted metasurface's pose, and measures the magnitude and phase of S_{21}. Timing measurements are recorded to ensure synchronization between the Vicon and VNA data streams, as reported in Algorithm 1. All acquired data, including timestamps, frequencies, S_{21} parameters, positions, and poses, are stored in an output file.

VI. TEST PROCEDURE AND OBTAINED RESULTS

The system parameters used in the analysis are described in Table II. To characterize the real-world behavior of APM, the experimental setup depicted in Fig. 4 was designed and implemented. The experimental setup consists of two horn antennas separated by a distance d: the Tx (i.e., the blue one), positioned perpendicular to the metasurface, and the Rx (i.e. the red one), tilted at a certain angle θ = 52° to the ground. It is important to highlight that these roles (Tx/Rx) are interchangeable due to the reciprocity of the metasurface. Moreover, h represents the height of the metasurface above the Tx.

A. Fixed-PM characterization

The measurement setup is reported in Fig. 5. The initial characterization involved validating the PM behavior by analyzing the scattering parameter S_{21} variations across different θ. The PM was fixed at h = 60 cm, with a fixed Tx-Rx separation distance d = 76 cm. We compared these measurements against results obtained using a copper foil as a reference. As shown in Fig. 6 (a), the fixed-PM significantly enhanced S_{21} intensity as the antenna inclination θ increased, reaching a peak at θ = 50° at a frequency of 9.76 GHz. Beyond this angle θ, S_{21} decreases until reaching θ = 70°, where Fabry-Perot resonances emerged due to reflections from the Tx. In contrast, the reference copper foil, acting as a mirror, consistently exhibited low S_{21} intensity across all Rx angles and frequencies. The maximum S_{21} value measured with the copper foil was equal to -35.6 dB at 8.12 GHz, which remained approximately 12 dB lower than the maximum value observed with the PM.

Moreover, the characterization of the fixed-PM also considered the following parameters:

- h ranging from 0 to 120 cm;
- d ranging from 40 to 100 cm;
- Tx position varied along both x and y axes of the metasurface.

The S_{21} intensity was investigated as h and d were varied. The results are depicted in Fig. 6 (b) and (c), respectively. As h increased (see Fig. 6 (b)), the maximum S_{21} shifted towards higher frequencies, with the peak value equal to -22.49 dB, occurring at h = 57 cm above Tx at the frequency of 9.76 GHz. Moreover, as the distance d between Tx and Rx varied (see Fig. 6 (c)), higher S_{21} values were observed in the range between 60 and 80 cm. The maximum value (-23.55 dB) was obtained at 9.88 GHz when d = 65.8 cm. Additionally, a secondary maximum appears for smaller values of d and frequency, probably due to a secondary lobe of Tx reflected toward Rx. Finally, to determine the region extent in which the UAV can fly around Tx during the APM characterization, an analysis was performed by varying the position of Tx along the parallel and perpendicular axes of the metasurface. The results are reported in Fig. 6 (d) and (e), respectively. In the case of shift along the y-axis of Tx (see Fig. 6 (d)), the analysis was performed by moving the antenna 10 cm in both the positive and negative directions of the y-axis with respect to the center of the metasurface. The results show a maximum in S_{21} at 9.54 GHz with an amplitude of -23.99 dB. This value decreases when the antenna is moved along the positive y-axis, and the maximum is obtained at progressively lower frequencies. In the case of shift along the x-axis of the Tx (see Fig. 6 (e)), the maximum value of the S_{21} parameter, equal to -23.89 dB at 9.86 GHz, is obtained at its initial position, at the center of the metasurface. As the displacement from the center increases, the S_{21} value gradually decreases. Moreover, the spectrum clearly reveals the metasurface reciprocal behavior. Furthermore, to estimate the optimal 3D APM flight space, the intensity of the signal received by Rx was analyzed by changing its horizontal (ϕ) and vertical (θ) angles of inclination. Specifically, ϕ was varied from -45° to 45°, while θ was varied from 0° to 70°. This approach enabled the reconstruction of the 2D color map presented in Fig. 6 (f), which shows that the receiving antenna aperture angle is approximately 30°.

B. Pose impact on electromagnetic behavior

In Fig. 9 is reported an example of APM measure.

1) Fixed-PM: The analysis of Fig. 7 (a) reveals that the absolute maximum of S_{21} occurs as θ_r decreases, with a corresponding increase in frequency. Conversely, as θ_r increases, the maximum shifts to lower frequencies. This trend is consistent: an increase in θ_r causes the S_{21} peak to shift downward in frequency, whereas a decrease θ_r shifts the peak toward higher frequencies. Regarding the variation of θ_p , the system exhibits lower sensitivity. As shown in Fig. 7 (b), within the range of -4° to 2°, the S_{21} value remains nearly constant. A signal loss is observed only for angles exceeding 2°. This behavior aligns with theoretical expectations since small inclinations of the metasurface relative to θ_p have minimal impact on performance. Specifically, the variation of the angle θ_p modulates the projected length of the wavevector $\mathbf{k}$ along the axis of variation of the metasurface elements. However, for small fluctuations of θ_p , this projected length remains nearly invariant. The maximum S_{21} value is consistently found within the 10–11 GHz range, with the highest measured value at 10.32 GHz corresponding to θ_p = 0°.

2) APM: To further deepen the comparative analysis between Fixed-PM and APM tests, flights were performed with the UAV hovering in the proximity of a fixed position aligned with the Tx antenna at the optimal height, as determined by the Fixed-PM tests shown in Fig. 6 (b). This test investigated the impact of UAV wobbling on the electromagnetic response. As shown in Fig. 8 (a), the S_{21} values remain largely consistent over time, with only minor variations. Recorded tilt values of the UAV-metasurface are as follows (see Fig. 8 (b)): θ_y ranged between 1.4° and 0°, θ_p between 0.88° and -0.86°, and θ_r between 1.12° and -2.46°. In terms of positional shifts, $s_{m,x}$ varied between 3.05 cm and -2.58 cm, $s_{m,y}$ between 3.75 cm and -3.30 cm, and $s_{m,z}$ between 1.75 cm and -1.87 cm, as reported in Fig. 8 (c).

C. Comparative analysis on APM and Fixed-PM

We varied the APM's height (along the z-axis) from 0 cm to 120 cm and compared these measurements with the fixed-PM results. As shown in Fig. 10, results demonstrate good agreement between both configurations. The maximum of S_{21}, equal to -23.49 dB, was observed at a height of 52 cm and a frequency of 9.75 GHz, whereas in the fixed-PM case, a maximum of -23.3 dB occurred at 51 cm at the same operating frequency.

After determining the optimal height, we analyzed the impact of the UAV's displacement along both the y-axis and z-axis. For y-axis displacement (as shown in Fig. 11), the comparison shows that as the displacement along the positive

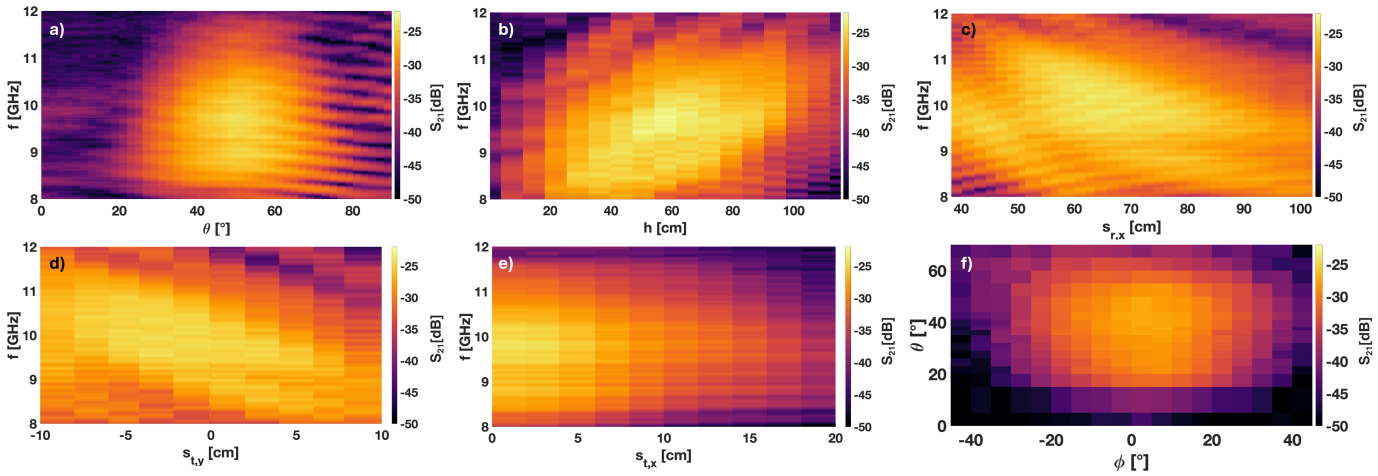

Fig. 6. Fixed-metasurface S_{21} characterization: variation of (a) the inclination angle θ, (b) the height h of the metasurface above the Tx, (c) the distance d between Tx and Rx, (d, e) the shift along the (d) y-axis and (e) x-axis, and (f) the inclination angles θ and ϕ of the Rx.

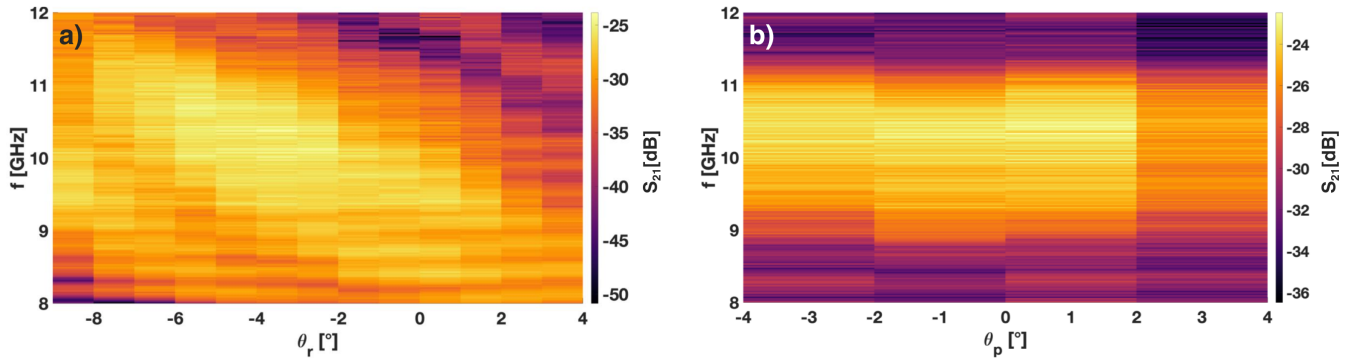

Fig. 7. S_{21} intensity (in dB) due to the variation of fixed-PM system angles: (a) θ_r and (b) θ_p .

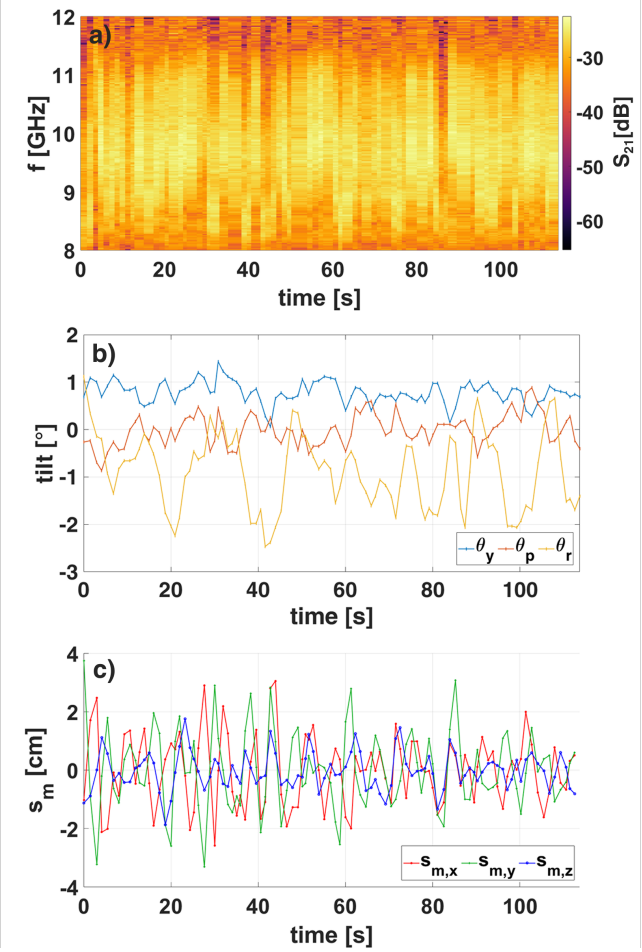

Fig. 8. UAV Wobbling in hovering condition: (a) the variation of S_{21} as a function of frequency. (b,c) The APM (b) tilt and (c) position shift over time.

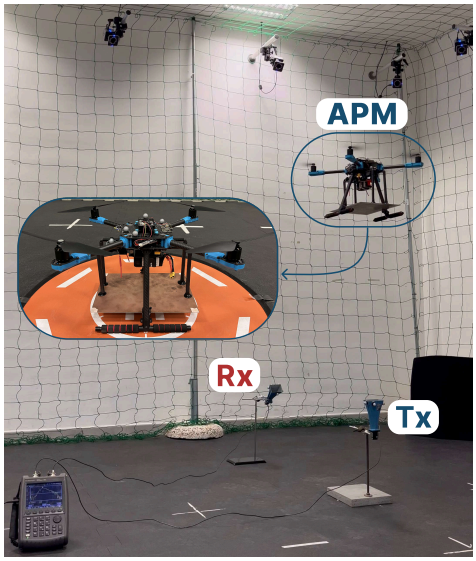

Fig. 9. Photo of the setup implemented for the APM measurements with a magnified detail of the metasurface mounted on the UAV.

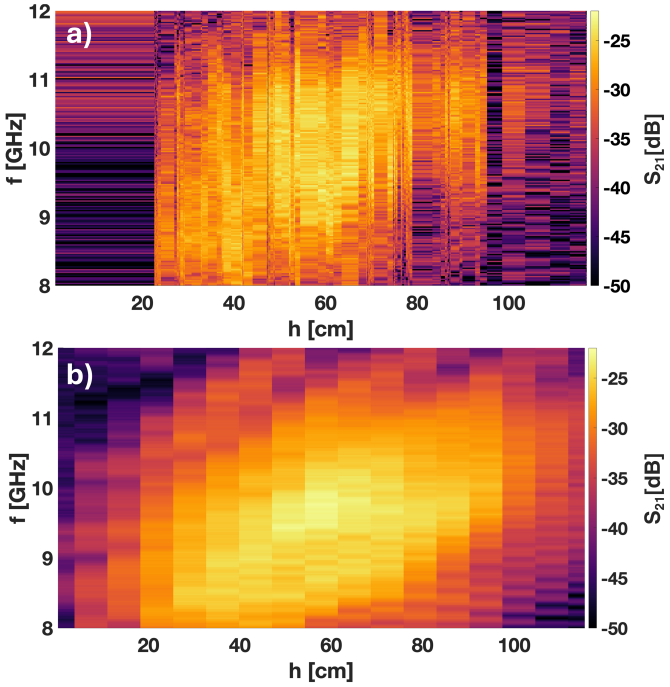

Fig. 10. Comparison between the S_{21} characterization of (a) APM and (b) fixed-PM systems for different values of h.

y-direction increased from 0 cm, the maximum S_{21} shifted to higher frequencies. Under fixed-PM conditions, the maximum S_{21} was -24.35 dB at 9.75 GHz for a zero displacement, while in the APM scenario, the maximum was -24.6 dB at 9.75 GHz for the same displacement along the y-axis.

Finally, for displacement along the x-axis of the Tx as shown in Fig. 12, the maximum S_{21} remained nearly constant within the range of 0 to 5 cm in both fixed-PM and APM conditions. Under fixed-PM (APM) conditions, the maximum S_{21} was -23.82 dB (-25.03 dB) at 9.75 GHz when the metasurface was aligned with the center of the Tx antenna.

D. Spatial radio environment characterization

After specifically characterizing the electromagnetic behavior of the metasurface for each axis, the overall study in three-dimensional space is highlighted in Fig. 13. In particular, multiple flight tests were performed to characterize a three-dimensional space environment map to understand the areas where S_{21} values are acceptable. A selective filtering criterion was applied to the measurement dataset to enhance the clarity and reliability of the presented results. Specifically, only measurements satisfying $S_{21} >$ -40 dB were considered, while the angular constraints were set to $\theta_y \in [-3.5°, 3.5°]$ and $\theta_r \in [-0.5°, 1.5°]$. This filtering process ensures the analysis focuses on stable and representative measurement conditions.

Fig. 13 illustrates the electromagnetic distribution through multiple views: (a) depicts the xy-plane slice where the maximum S_{21} value of -22.48 dB at 9.7 GHz is centered at the Tx antenna position; (b) and (c) show, the xz-plane and yz-plane slices respectively, both confirming that the peak S_{21} occurs directly above the Tx antenna at h = 57 cm, which validates the findings in Fig. 10 (a). Fig. 13 (d) provides a comprehensive 3D visualization of the electromagnetic field

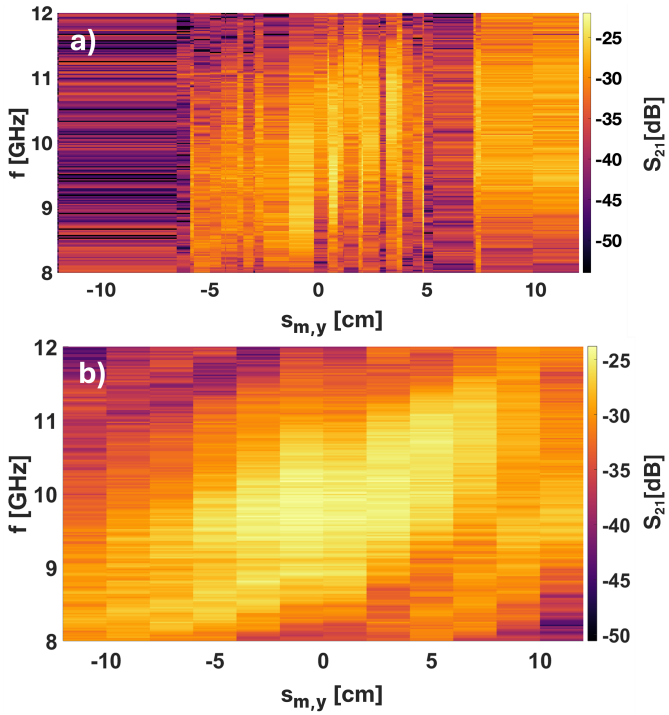

Fig. 11. Comparison between the S_{21} characterization of (a) APM and (b) fixed-PM systems, by varying the displacement of the metasurface along the y-axis.

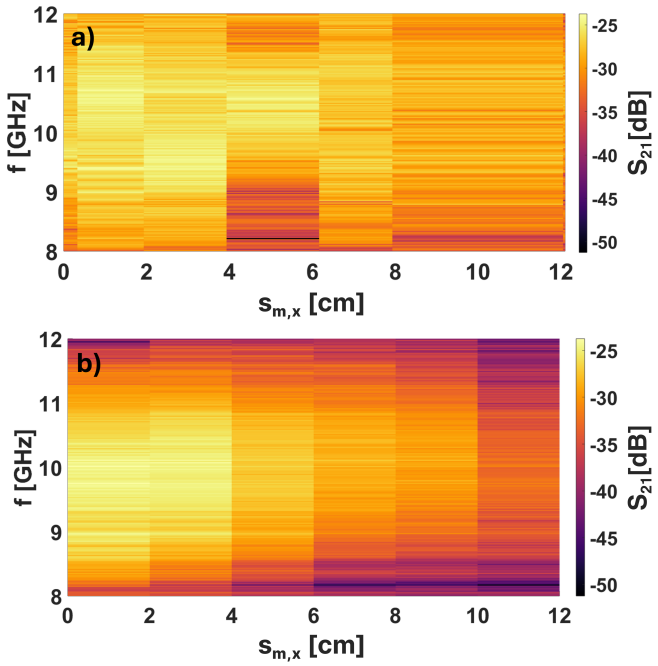

Fig. 12. Comparison between (a) APM and (b) fixed-PM characterization by varying the displacement of the metasurface along the x-axis.

strength, highlighting the effective region where S_{21} exceeds -35 dB, which spans a volume of 24 cm × 35 cm × 69 cm, considering the Tx as the origin.

This analysis provides valuable insights into the system's radio environment map to develop algorithms for automated control, ensuring optimal UAV positioning on nodes so that LOS communication is always maintained, even in the presence of obstacles.

E. Evaluation and Final Considerations

The experimental evaluation conducted in this study highlights the feasibility and potential of APMs for enhancing indoor wireless communication. Our analysis, based on a fully integrated testbed combining UAV pose tracking with real-time electromagnetic measurements, provides valuable insights into the practical challenges and benefits of APM deployment.

The comparative study between fixed-PM and APM setups reveals that while both configurations significantly improve signal strength and spectral efficiency, APMs introduce additional complexities due to UAV-induced motion effects, including wobbling, and positional drifts. In particular, when the UAV remains in a fixed position, the orientation angles fluctuate within the following ranges: θ_r varies between -2.5° and 0.8°, θ_p ranges from -0.9° to 0.7°, and θ_y oscillates between 0° and 1.3°.

Moreover, by considering positional drifts in conjunction with wobbling, it can be observed that, apart from minor frequency shifts, the received signal experiences minimal losses if the APM moves relative to the transmitter by 24 cm along the x-axis, 35 cm along the y-axis, and 69 cm along the z-axis. Experimental results indicate that these factors cause fluctuations in the electromagnetic response of the APM, providing a foundation for developing autonomous UAV positioning algorithms in warehouse or industrial environments.

Furthermore, improper UAV orientation can degrade link performance, leading to frequency shifts in the peak of the S_{21} parameter and, consequently, a reduction in received power and potential information loss. To mitigate these issues, a real-time control system [36] can be implemented on the UAV to maximize the S_{21} value by leveraging orientation and positional feedback. Moreover, the sensitivity of the APM to pose variation can be exploited to enable power-based adaptive retransmission algorithms or real-time repositioning strategies aimed at dynamically restoring LOS conditions in cluttered environments. A promising solution involves the integration of an electromechanical gimbal [51], which stabilizes the metasurface by reducing vibrations and maintaining optimal alignment with both the transmitter and the receiver.

Moreover, this analysis suggests that these effects should also be considered in the design of metasurfaces suitable for these kinds of applications.

F. Future perspectives

Although this study focuses on indoor scenarios representative of warehouse environments, preliminary measurements were additionally conducted outdoors under controlled conditions, in the absence of rain or strong wind. The same

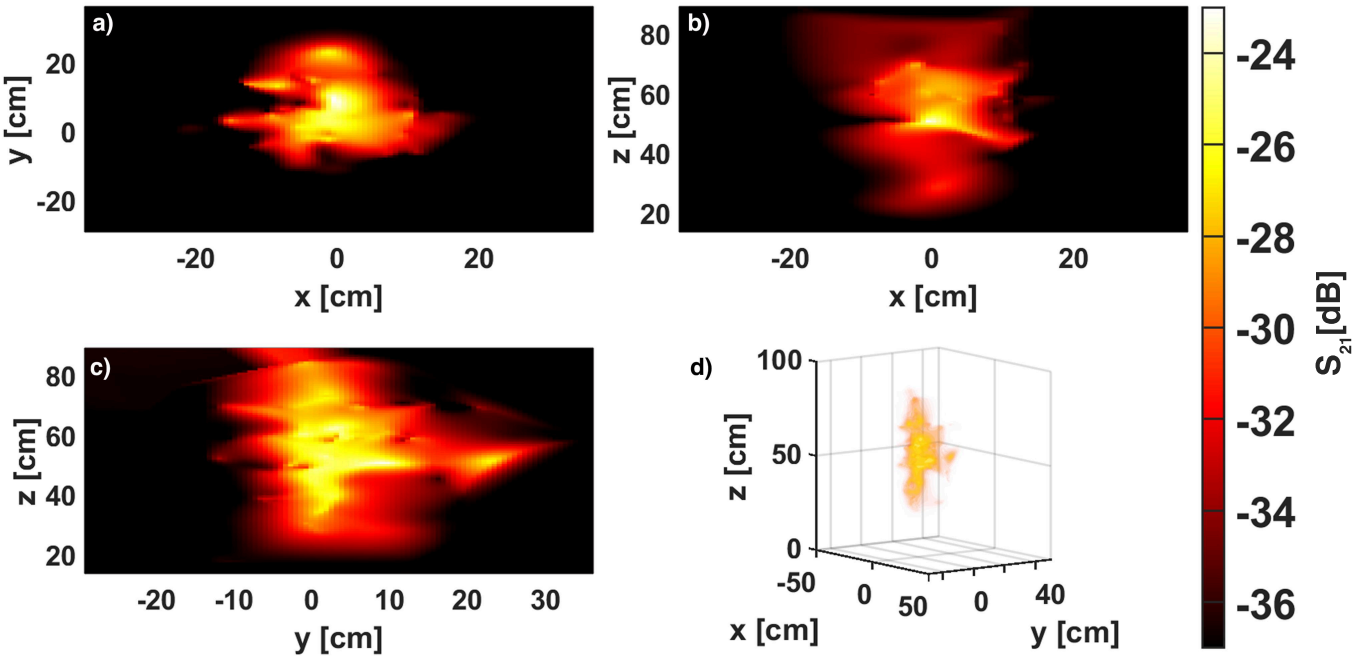

Fig. 13. Different cutting-planes of the (a) xy-axes, (b) xz-axes, (c) yz-axes and (d) 3D spatial characterization of S_{21} through several APM measurements.

experimental setup used for indoor trials was retained: the transmitting and receiving horn antennas were kept at a fixed separation of 76 cm, and the Passive Metasurface (PM) was mounted 60 cm above the Transmitting (TX) antenna. Comparison of indoor and outdoor measurements indicates good agreement. In the indoor case, the S_{21} peak was -23.98 dB at 9.75 GHz, whereas outdoor it reached -24.45 dB at 9.78 GHz. This corresponds to a 30 MHz shift, likely due to minor misalignment or light wind. Future work will extend this analysis by considering different PM placements and heights on the TX antenna."

Moreover, this activity could be further expanded by utilizing Intelligent Reflective Surfaces (IRSs) instead of PMs. These programmable metasurfaces would offer dynamic control over beam direction but introduce trade-offs in terms of power consumption, weight, and system complexity, especially for UAV deployment. Therefore, a cost-benefit analysis is essential to assess their feasibility in real-world scenarios where energy autonomy and weight are critical constraints.This investigation would tackle new research challenges, including the assessment of environmental impacts on PM performance in dynamic, complex outdoor scenarios and the mitigation of electromagnetic interference.

VII. Conclusions

Aerial Intelligent Reflective Surfaces (AIRSs) and Aerial Passive Metasurfaces (APMs) are emerging as a groundbreaking solution for dynamically reshaping the wireless environment, significantly improving coverage and communication efficiency.

In this paper, we present a pioneering real-world study on the performance of Unmanned Aerial Vehicle (UAV)-assisted metasurfaces for indoor communications. To this end, we developed a fully integrated experimental testbed that combines a Vicon motion capture system with a Vector Network Analyzer (VNA). At the core of our setup is a customized Real-Time Vicon-VNA Collector Module, which enables seamless synchronization between UAV pose tracking and electromagnetic measurements.

For the first time in the literature, we provide a comprehensive experimental characterization of how UAV movement and vibration influence the electromagnetic response in an indoor environment, specifically tailored for warehouse applications. Our findings reveal that while UAV-assisted metasurfaces significantly enhance received electromagnetic power, their effectiveness is highly dependent on precise positioning, orientation relative to the transmitting and receiving antennas, and flight stability.

This in-depth characterization establishes a solid foundation for optimizing and planning AIRS-assisted communications more efficiently. Moreover, our results emphasize the need for metasurface designs with enhanced resilience to UAV-induced wobbling, pushing the boundaries of future innovations in this field.

Looking ahead, our experimental setup can be extended to more challenging outdoor scenarios, facilitating seamless integration between terrestrial and non-terrestrial networks. Additionally, future work may explore UAV-assisted swarms and introduce reconfigurability into metasurface design, unlocking additional potential for next-generation wireless communication systems. To advance the field and address the complexities of real-world applications, key challenges remain:

- quantifying the effect of varying environmental conditions (e.g., temperature and humidity) on metasurface performance;
- exploring the integration of IRSs for adaptive beamforming and network optimization in real-time;

- developing energy-efficient IRS solutions for UAVs in extended flights;
- ensuring robustness against electromagnetic interference, dynamic obstacles, and urban clutter.

REFERENCES

[1] Y. Liu, X. Liu, X. Mu, T. Hou, J. Xu, M. Di Renzo, and N. Al-Dhahir, "Reconfigurable intelligent surfaces: Principles and opportunities," *IEEE Communications Surveys & Tutorials*, vol. 23, no. 3, pp. 1546–1577, 2021.

[2] Y. Zeng, Q. Wu, and R. Zhang, "Accessing from the sky: A tutorial on uav communications for 5g and beyond," *Proceedings of the IEEE*, vol. 107, no. 12, pp. 2327–2375, 2019.

[3] J. Ye, J. Qiao, A. Kammoun, and M.-S. Alouini, "Nonterrestrial communications assisted by reconfigurable intelligent surfaces," *Proceedings of the IEEE*, vol. 110, no. 9, pp. 1423–1465, 2022.

[4] R. Luo, W. Ni, H. Tian, and J. Cheng, "Federated deep reinforcement learning for ris-assisted indoor multi-robot communication systems," *IEEE Transactions on Vehicular Technology*, vol. 71, no. 11, pp. 12 321–12 326, 2022.

[5] S. Alfattani, W. Jaafar, Y. Hmamouche, H. Yanikomeroglu, A. Yongaçoglu, N. D. Dào, and P. Zhu, "Aerial platforms with reconfigurable smart surfaces for 5g and beyond," *IEEE Communications Magazine*, vol. 59, no. 1, pp. 96–102, 2021.

[6] L. Ge, P. Dong, H. Zhang, J.-B. Wang, and X. You, "Joint beamforming and trajectory optimization for intelligent reflecting surfaces-assisted uav communications," *IEEE Access*, vol. 8, pp. 78 702–78 712, 2020.

[7] S. Gong, X. Lu, D. T. Hoang, D. Niyato, L. Shu, D. I. Kim, and Y.-C. Liang, "Toward smart wireless communications via intelligent reflecting surfaces: A contemporary survey," *IEEE Communications Surveys & Tutorials*, vol. 22, no. 4, pp. 2283–2314, 2020.

[8] P. Mursia, F. Devoti, V. Sciancalepore, and X. Costa-Pérez, "Rise of flight: Ris-empowered uav communications for robust and reliable air-to-ground networks," *IEEE Open Journal of the Communications Society*, vol. 2, pp. 1616–1629, 2021.

[9] Q. Zhang, W. Saad, and M. Bennis, "Reflections in the sky: Millimeter wave communication with uav-carried intelligent reflectors," in *2019 IEEE Global Communications Conference (GLOBECOM)*, 2019, pp. 1–6.

[10] S. Kayraklık, I. Yildirim, Y. Gevez, E. Basar, and A. Görçin, "Indoor coverage enhancement for ris-assisted communication systems: Practical measurements and efficient grouping," in *ICC 2023 - IEEE International Conference on Communications*, 2023, pp. 485–490.

[11] A. Araghi, M. Khalily, M. Safaei, A. Bagheri, V. Singh, F. Wang, and R. Tafazolli, "Reconfigurable intelligent surface (ris) in the sub-6 ghz band: Design, implementation, and real-world demonstration," *IEEE Access*, vol. 10, pp. 2646–2655, 2022.

[12] J. Rains, J. ur Rehman Kazim, A. Tukmanov, T. J. Cui, L. Zhang, Q. H. Abbasi, and M. A. Imran, "High-resolution programmable scattering for wireless coverage enhancement: An indoor field trial campaign," *IEEE Transactions on Antennas and Propagation*, vol. 71, no. 1, pp. 518–530, 2023.

[13] A. Benoni, F. Capra, M. Salucci, and A. Massa, "Toward real-world indoor smart electromagnetic environments—a large-scale experimental demonstration," *IEEE Transactions on Antennas and Propagation*, vol. 71, no. 11, pp. 8450–8463, 2023.

[14] X. Pang, M. Sheng, N. Zhao, J. Tang, D. Niyato, and K.-K. Wong, "When uav meets irs: Expanding air-ground networks via passive reflection," *IEEE Wireless Communications*, vol. 28, no. 5, pp. 164–170, 2021.

[15] J. Li and J. Liu, "Sum rate maximization via reconfigurable intelligent surface in uav communication: Phase shift and trajectory optimization," in *2020 IEEE/CIC International Conference on Communications in China (ICCC)*, 2020, pp. 124–129.

[16] H. Mei, K. Yang, Q. Liu, and K. Wang, "3d-trajectory and phase-shift design for ris-assisted uav systems using deep reinforcement learning," *IEEE Transactions on Vehicular Technology*, vol. 71, no. 3, pp. 3020–3029, 2022.

[17] L. Wang, K. Wang, C. Pan, and N. Aslam, "Joint trajectory and passive beamforming design for intelligent reflecting surface-aided uav communications: A deep reinforcement learning approach," *IEEE Transactions on Mobile Computing*, vol. 22, no. 11, pp. 6543–6553, 2023.

[18] Z. Wei, Y. Cai, Z. Sun, D. W. K. Ng, J. Yuan, M. Zhou, and L. Sun, "Sum-rate maximization for irs-assisted uav ofdma communication systems," *IEEE Transactions on Wireless Communications*, vol. 20, no. 4, pp. 2530–2550, 2021.

[19] X. Liu, Y. Liu, and Y. Chen, "Machine learning empowered trajectory and passive beamforming design in uav-ris wireless networks," *IEEE Journal on Selected Areas in Communications*, vol. 39, no. 7, pp. 2042–2055, 2021.

[20] A. Bansal, N. Agrawal, and K. Singh, "Rate-splitting multiple access for uav-based ris-enabled interference-limited vehicular communication system," *IEEE Transactions on Intelligent Vehicles*, vol. 8, no. 1, pp. 936–948, 2023.

[21] X. Guo, Y. Chen, and Y. Wang, "Learning-based robust and secure transmission for reconfigurable intelligent surface aided millimeter wave uav communications," *IEEE Wireless Communications Letters*, vol. 10, no. 8, pp. 1795–1799, 2021.

[22] Y. Pan, K. Wang, C. Pan, H. Zhu, and J. Wang, "Uav-assisted and intelligent reflecting surfaces-supported terahertz communications," *IEEE Wireless Communications Letters*, vol. 10, no. 6, pp. 1256–1260, 2021.

[23] S. Li, B. Duo, M. D. Renzo, M. Tao, and X. Yuan, "Robust secure uav communications with the aid of reconfigurable intelligent surfaces," *IEEE Transactions on Wireless Communications*, vol. 20, no. 10, pp. 6402–6417, 2021.

[24] Z. Mohamed and S. Aïssa, "Leveraging uavs with intelligent reflecting surfaces for energy-efficient communications with cell-edge users," in *2020 IEEE International Conference on Communications Workshops (ICC Workshops)*, 2020, pp. 1–6.

[25] H. Lu, Y. Zeng, S. Jin, and R. Zhang, "Aerial intelligent reflecting surface: Joint placement and passive beamforming design with 3d beam flattening," *IEEE Transactions on Wireless Communications*, vol. 20, no. 7, pp. 4128–4143, 2021.

[26] X. Liu, Y. Yu, F. Li, and T. S. Durrani, "Throughput maximization for ris-uav relaying communications," *IEEE Transactions on Intelligent Transportation Systems*, vol. 23, no. 10, pp. 19 569–19 574, 2022.

[27] H. Peng, L.-C. Wang, G. Ye Li, and A.-H. Tsai, "Long-lasting uav-aided ris communications based on swipt," in *2022 IEEE Wireless Communications and Networking Conference (WCNC)*, 2022, pp. 1844–1849.

[28] H. Long, M. Chen, Z. Yang, Z. Li, B. Wang, X. Yun, and M. Shikh-Bahaei, "Joint trajectory and passive beamforming design for secure uav networks with ris," in *2020 IEEE Globecom Workshops (GC Wkshps*, 2020, pp. 1–6.

[29] Z. Hou, J. Chen, Y. Huang, Y. Luo, X. Wang, J. Gu, Y. Xu, and K. Yao, "Joint trajectory and passive beamforming optimization in irs-uav enhanced anti-jamming communication networks," *China Communications*, vol. 19, no. 5, pp. 191–205, 2022.

[30] X. Tang, D. Wang, R. Zhang, Z. Chu, and Z. Han, "Jamming mitigation via aerial reconfigurable intelligent surface: Passive beamforming and deployment optimization," *IEEE Transactions on Vehicular Technology*, vol. 70, no. 6, pp. 6232–6237, 2021.

[31] H. Zhang, M. Huang, H. Zhou, X. Wang, N. Wang, and K. Long, "Capacity maximization in ris-uav networks: A ddqn-based trajectory and phase shift optimization approach," *IEEE Transactions on Wireless Communications*, vol. 22, no. 4, pp. 2583–2591, 2023.

[32] S. Jiao, X. Xie, and Z. Ding, "Deep reinforcement learning-based optimization for ris-based uav-noma downlink networks," *Frontiers in Signal Processing*, vol. 2, 2022.

[33] S. Jiao, F. Fang, X. Zhou, and H. Zhang, "Joint beamforming and phase shift design in downlink uav networks with irs-assisted noma," *Journal of Communications and Information Networks*, vol. 5, no. 2, pp. 138–149, 2020.

[34] L. Yang, P. Li, F. Meng, and S. Yu, "Performance analysis of ris-assisted uav communication systems," *IEEE Transactions on Vehicular Technology*, vol. 71, no. 8, pp. 9078–9082, 2022.

[35] T. Shafique, H. Tabassum, and E. Hossain, "Optimization of wireless relaying with flexible uav-borne reflecting surfaces," *IEEE Transactions on Communications*, vol. 69, no. 1, pp. 309–325, 2021.

[36] H. Zhao, W. Sun, Y. Ni, W. Xia, G. Gui, and C. Zhu, "Deep deterministic policy gradient-based rate maximization for ris-uav-assisted vehicular communication networks," *IEEE Transactions on Intelligent Transportation Systems*, vol. 25, no. 11, pp. 15 732–15 744, 2024.

[37] Y. M. Park, Y. K. Tun, Z. Han, and C. S. Hong, "Trajectory optimization and phase-shift design in irs-assisted uav network for smart railway," *IEEE Transactions on Vehicular Technology*, vol. 71, no. 10, pp. 11 317–11 321, 2022.

[38] X. Liu, Y. Yu, B. Peng, X. B. Zhai, Q. Zhu, and V. C. M. Leung, "Ris-uav enabled worst-case downlink secrecy rate maximization for mobile

vehicles," *IEEE Transactions on Vehicular Technology*, vol. 72, no. 5, pp. 6129–6141, 2023.

[39] B. Yu, J. Zhang, J. Chen, Y. Xu, R. Gao, and J. Wang, "Aerial ris-enabled wireless coverage enhancement under uav jitter," in *2023 IEEE 23rd International Conference on Communication Technology (ICCT)*, 2023, pp. 1712–1716.

[40] M. Al-Jarrah, A. Al-Dweik, E. Alsusa, Y. Iraqi, and M.-S. Alouini, "On the performance of irs-assisted multi-layer uav communications with imperfect phase compensation," *IEEE Transactions on Communications*, vol. 69, no. 12, pp. 8551–8568, 2021.

[41] M. Al-Jarrah, E. Alsusa, A. Al-Dweik, and D. K. C. So, "Capacity analysis of irs-based uav communications with imperfect phase compensation," *IEEE Wireless Communications Letters*, vol. 10, no. 7, pp. 1479–1483, 2021.

[42] Z. Wang, J. Bian, C.-X. Wang, Y. Liu, and J. Tian, "Aerial reconfigurable intelligent surface-assisted channel modeling incorporating the effect of uav fluctuations," *IEEE Communications Letters*, vol. 28, no. 7, pp. 1599–1603, 2024.

[43] P.-V. Mekikis, D. Tyrovolas, S. Tegos, A. Papadopoulos, A. Pitilakis, S. Ioannidis, A. Tsioliaridou, P. Diamantoulakis, N. Kantartzis, G. Karagiannidis, and C. Liaskos, "Dynamic programmable wireless environment with uav-mounted static metasurfaces," in *2022 IEEE Conference on Standards for Communications and Networking (CSCN)*, 2022, pp. 101–104.

[44] W. Tang, M. Z. Chen, X. Chen, J. Y. Dai, Y. Han, M. Di Renzo, Y. Zeng, S. Jin, Q. Cheng, and T. J. Cui, "Wireless communications with reconfigurable intelligent surface: Path loss modeling and experimental measurement," *IEEE Transactions on Wireless Communications*, vol. 20, no. 1, pp. 421–439, 2021.

[45] A. Pitilakis, D. Tyrovolas, P.-V. Mekikis, S. A. Tegos, A. Papadopoulos, A. Tsioliaridou, O. Tsilipakos, D. Manessis, S. Ioannidis, N. V. Kantartzis, I. F. Akyildiz, and C. K. Liaskos, "On the mobility effect in uav-mounted absorbing metasurfaces: A theoretical and experimental study," *IEEE Access*, vol. 11, pp. 79 777–79 792, 2023.

[46] I.Marasco, C. Cantore, G. V. Bianco, G.Bruno, A. D'orazio, and G.Magno, "Transparent graphene-based ris for 6g communications in the thz spectrum," *IEEE Open Journal of Antennas and Propagation*, pp. 1–1, 2024.

[47] Dassault Systemes, "CST Studio Suite: Electromagnetic Field Simulation Software," https://www.3ds.com/products-services/simulia/products/cst-studio-suite/, 2025, accessed: 2025-02-19.

[48] Tridge and contributors, "pyvicon: Python interface for vicon motion capture systems," https://github.com/tridge/pyvicon, 2018-02-01, accessed: 2025-02-18.

[49] A. D. Team, *MAVProxy: A fully-functional GCS for ArduPilot*, https://ardupilot.org/mavproxy/index.html, 2024-09-09, accessed: 2025-02-18.

[50] P. Merriaux, Y. Dupuis, R. Boutteau, P. Vasseur, and X. Savatier, "A study of vicon system positioning performance," *Sensors*, vol. 17, no. 7, 2017. [Online]. Available: https://www.mdpi.com/1424-8220/17/7/1591

[51] Y. Liu, B. Duo, Q. Wu, X. Yuan, J. Li, and Y. Li, "Elevation angle-dependent 3d trajectory design for aerial ris-aided communication," *IEEE Transactions on Intelligent Transportation Systems*, vol. 25, no. 3, pp. 2696–2702, 2024.